

THE ACCELERATION OF ENERGETIC PARTICLES AT CORONAL SHOCKS AND EMERGENCE OF A DOUBLE POWER LAW FEATURE IN PARTICLE ENERGY SPECTRA

XIANGLIANG KONG,^{1,2} FAN GUO,^{3,4} YAO CHEN,¹ AND JOE GIACALONE⁵

¹*Shandong Provincial Key Laboratory of Optical Astronomy and Solar-Terrestrial Environment, and Institute of Space Sciences, Shandong University, Weihai, Shandong 264209, China; kongx@sdu.edu.cn*

²*Sate Key Laboratory of Space Weather, Chinese Academy of Sciences, Beijing 100190, China*

³*Los Alamos National Laboratory, Los Alamos, NM 87545, USA*

⁴*New Mexico Consortium, Los Alamos, NM 87544, USA*

⁵*Department of Planetary Sciences, University of Arizona, Tucson, AZ 85721, USA*

ABSTRACT

We present numerical modelling of particle acceleration at coronal shocks propagating through a streamer-like magnetic field by solving the Parker transport equation with spatial diffusion both along and across the magnetic field. We show that the location on the shock where the high-energy particle intensity is the largest, depends on the energy of the particles and on time. The acceleration of particles to more than 100 MeV mainly occurs in the shock-streamer interaction region, due to perpendicular shock geometry and the trapping effect of closed magnetic fields. A comparison of the particle spectra to that in a radial magnetic field shows that the intensity at 100 MeV (200 MeV) is enhanced by more than one order (two orders) of magnitude. This indicates that the streamer-like magnetic field can be an important factor in producing large solar energetic particle events. We also show that the energy spectrum integrated over the simulation domain consists of two different power laws. Further analysis suggests that it may be a mixture of two distinct populations accelerated in the streamer and open field regions, where the acceleration rate differs substantially. Our calculations also show that the particle spectra are affected considerably by a number of parameters, such as the streamer tilt angle, particle spatial diffusion coefficient, and shock compression ratio. While the low-energy spectra agree well with standard diffusive shock acceleration theory, the break energy ranges from ~ 1 MeV to ~ 90 MeV and the high-energy spectra can extend to ~ 1 GeV with a slope of $\sim 2-3$.

Keywords: acceleration of particles — shock waves — Sun: corona — Sun: coronal mass ejections (CMEs) — Sun: magnetic fields — Sun: particle emission

1. INTRODUCTION

Charged particles can be accelerated to energies beyond a few GeV near the Sun during large solar eruptions such as flares and coronal mass ejections (CMEs) (see reviews, [Reames 1999](#); [Desai & Giacalone 2016](#)). Large solar energetic particle (SEP) events are usually defined as the proton flux in the >10 MeV *GOES* energy channel exceeding $10 \text{ particle cm}^{-2} \text{ s}^{-1} \text{ sr}^{-1}$ (particle flux unit, pfu) and there have been about 10 events observed per year during solar maximum. Those events are of particular interest to space weather because of their severe radiation threats to human activities in space. In some extreme SEP events, so-called ground level enhancements (GLEs), the \sim GeV ions can produce sufficient secondary particles detectable by ground-based neutron monitors. There have been only 2 GLE events recorded in solar cycle 24 ([Gopalswamy et al. 2013a, 2018](#)), in comparison to 16 events in solar cycle 23. Although it is known that the solar activity is weak in this solar cycle, the physical reason for the lack of large SEP and GLE events remains unclear (see, e.g., [Gopalswamy et al. 2013a, 2014](#); [Giacalone 2015](#); [Mewaldt et al. 2015](#); [Vainio et al. 2017](#)).

In large SEP events, high-energy particles are generally believed to be accelerated by shock waves driven by fast CMEs ([Reames 1999](#); [Desai & Giacalone 2016](#)). Recent observations have shown that CME-driven shocks can form in the low corona and are capable of accelerating particles to high energies (see, e.g., [Bemporad & Mancuso 2010](#); [Ma et al. 2011](#); [Gopalswamy et al. 2012, 2013b](#)). Type II solar radio bursts are produced by electrons accelerated at shocks driven by solar eruptions ([Nelson & Melrose 1985](#)), and therefore they are commonly used as an indicator for the formation of shocks. [Gopalswamy et al. \(2013b\)](#) measured the leading edges or outermost fronts of CMEs at the starting time of associated Type II bursts for 32 events in solar cycle 24, and found that the shock can form at heights below $1.5 R_{\odot}$. For GLE events in solar cycle 23, [Gopalswamy et al. \(2012\)](#) showed that the shock formation heights deduced from the onset of Type II bursts are in the narrow range 1.3 to $1.8 R_{\odot}$, with a mean value of $\sim 1.5 R_{\odot}$, and the CME heights at GLE particle release range from 1.7 to $4 R_{\odot}$, with an average of $3.1 R_{\odot}$ for well-connected events (see also, [Reames 2009a,b](#)).

The primary acceleration region along the CME shock, i.e., where most of high-energy particles are produced, is a key issue that remains not well known. It has been shown that in large gradual

SEP events the main source of SEPs can be at both the shock nose (e.g., Cane et al. 1988; Reames et al. 1997; Lario et al. 2017) and the shock flank (e.g., Kahler 2016; Gopalswamy et al. 2018). The magnetic field configuration is of great importance for determining the primary acceleration region because the acceleration rate strongly depends on the angle θ_{Bn} between the upstream magnetic field and the shock normal. In the diffusive shock acceleration (DSA) theory, particles are accelerated more rapidly at a nearly perpendicular shock than at a parallel shock (Jokipii 1987; Giacalone 2005a,b). It is known that the magnetic field configuration in the corona is very complicated, consisting of large-scale closed field structures such as coronal loops and streamers. Therefore, when a CME-driven shock forms in the corona, the shock angles along the nonplanar front can vary significantly as it sweeps through the coronal magnetic field (e.g., Kozarev et al. 2013; Schwadron et al. 2015), resulting in different particle acceleration rates (e.g., Giacalone 2005a,b; Tylka et al. 2005; Tylka & Lee 2006). In this study, we will emphasize the importance of coronal magnetic field configuration for particle acceleration at CME-driven shocks.

In the solar corona, streamers are the most prominent quasi-steady structures and CMEs commonly interact with streamers as they expand or move outward (e.g., Chen et al. 2010; Feng et al. 2011). Recent observations have shown that Type II bursts are often associated with the interaction between shocks and streamers (e.g., Reiner et al. 2003; Mancuso & Raymond 2004; Cho et al. 2008; Feng et al. 2012, 2013; Kong et al. 2012, 2015; Chen et al. 2014) or the shock propagating through high-density coronal loops (e.g., Pohjolainen et al. 2008; Cho et al. 2013; Kumar et al. 2016). Kong et al. (2015, 2016) investigated the effect of a streamer-like magnetic field on electron acceleration at an outward-propagating coronal shock using test-particle simulations, and found that the primary electron acceleration region shifts as the shock propagates and the electron acceleration is more efficient when electrons are trapped in the closed field lines compared to electrons injected in open field regions.

However, it remains unclear what is the effect of streamers or CME/shock-streamer interaction on the acceleration, trapping and release of SEPs (see, e.g., Kahler et al. 2000; Kahler 2005; Rouillard et al. 2016; Kocharov et al. 2017). Kocharov et al. (2017) made detailed multi-wavelength analysis

of two GLE events, and suggested that relativistic protons initially accelerated during the flare and CME launch could be trapped in large-scale magnetic loops and later released by the expansion of CME and interaction of the CME with coronal streamers. A CME may originate below or outside of a streamer depending on the location of its active region, therefore the primary particle acceleration region (with perpendicular shock geometry) can occur both at the CME nose and flanks. The two GLE events in this solar cycle occurred on 2012 May 17 (Gopalswamy et al. 2013a; Shen et al. 2013; Rouillard et al. 2016) and 2017 September 10 (Cohen & Mewaldt 2018; Gopalswamy et al. 2018; Guo et al. 2018; Luhmann et al. 2018; Zhao et al. 2018b), respectively. In the first event the CME originated below the streamer belt (Rouillard et al. 2016), while in the second event the CME eruption region is located outside and near the edge of the streamer belt (Luhmann et al. 2018). Observations of CME/shock-streamer interaction for the two GLE events are presented in the Appendix.

Recently, Kong et al. (2017) presented a numerical model to investigate particle acceleration at CME-driven shocks close to the Sun, by considering a coronal shock with a kinematic description propagating through a streamer-like magnetic field that is analytically given (Low 1986). Particle acceleration is studied by solving the Parker transport equation (Parker 1965) with both parallel and perpendicular diffusion. They showed that particles can be sufficiently accelerated to above 100 MeV within $2\text{-}3 R_{\odot}$, and when the shock propagates through a streamer-like magnetic field, particles are more efficiently accelerated due to perpendicular shock geometry and the natural trapping effect of closed magnetic field lines. In this study, we further investigate the effect of large-scale streamer-like magnetic configuration on particle acceleration at coronal shocks when the CME-shock originates outside of the streamer and propagates through the streamer from the flank.

The rest of this paper is organized as follows. In Section 2, we describe the numerical model. In Section 3, we present the simulation results including the spatial distribution and energy spectra of accelerated particles. We also examine the effect of various parameters such as the diffusion coefficient on the particle energy spectra via a parameter study. In Section 4, we discuss the occurrence of double-power-law features in particle energy spectra. Conclusions are given in Section 5.

2. NUMERICAL MODEL

In this study, we further investigate the effect of large-scale streamer-like magnetic configuration on particle acceleration at coronal shocks using the numerical model developed by Kong et al. (2017). A schematic of the numerical model is shown in Figure 1. We consider a CME-driven shock originates outside of the streamer and propagates through the streamer from the flank. The outward-propagating coronal shock is represented by an expanding circular front. The background coronal magnetic field is taken to be an analytical solution of a streamer-like configuration (Low 1986). In the reference simulation, the streamer-like magnetic field is rotated by 45° toward the solar south pole, referred to as the streamer tilt angle Θ_{tilt} . We also examine the effect of Θ_{tilt} by considering the cases $\Theta_{tilt} = 30^\circ$ and 60° . The acceleration of protons in the shock-streamer system is modelled by numerically solving the Parker transport equation (Parker 1965) using a stochastic integration method (e.g., Guo et al. 2010; Senanayake & Florinski 2013; Li et al. 2018).

As shown in Figure 1, we use two coordinate systems simultaneously. In the heliocentric Cartesian coordinate system (x, y, z) , the origin is at the center of the Sun, with the z -axis being the solar rotation axis and the x -axis being toward the intersection of the solar equator and solar central meridian. Note that the analytic solution of the coronal magnetic field is axisymmetric about the solar rotation axis (Low 1986). We only consider a two-dimensional simulation in the x - z plane. In the shock coordinate system (R, Θ) in the x - z plane, the origin is set to be at the center of the shock. The R direction points outward radially from the shock center (i.e., along the shock normal), and Θ is defined as the angle with respect to the x axis and ranges from $-\pi/2$ to $\pi/2$.

We assume a circular shock front forms with an initial radius of $0.2 R_\odot$ (at $t = 0$) and moves outward with a constant speed $V_{sh} = 2000 \text{ km s}^{-1}$. The center of the shock is fixed in the solar equatorial plane at a height of $0.1 R_\odot$ above the solar surface, which is a reasonable assumption in the low corona region since the expansion is usually dominant in the initial phase of CMEs (e.g., Kwon et al. 2014; Liu et al. 2019). In recent observational studies, the density compression ratios along the shock fronts were deduced to be in the wide range of 1 to 3 (e.g., Bemporad & Mancuso 2010; Bemporad et al. 2014; Susino et al. 2015; Kwon & Vourlidas 2018). For the reference run, the

shock compression ratio X is 3. We also examine the effect of varying X and consider two other values, 2 and 2.5, respectively.

We describe the sharp variation in the shock layer by a hyperbolic tangent function. In local shock frame, the fluid velocity along the shock normal is given by,

$$U(x') = \frac{U_1 + U_2}{2} - \frac{U_1 - U_2}{2} \tanh\left(\frac{x'}{\delta_{sh}}\right), \quad (1)$$

where x' is the distance to the shock front along the shock normal, U_1 and U_2 are the upstream and downstream normal flow speeds, and δ_{sh} is the width of the shock. To obtain the correct solution of DSA, the width of the shock δ_{sh} should be much smaller than the characteristic diffusion length at the shock front $L_d = \kappa_{nn}/V_{sh}$, where κ_{nn} is the diffusion coefficient in the direction normal to the shock. We take $\delta_{sh} = 4 \times 10^{-5} R_\odot$ in our simulations to ensure that this condition is satisfied. Note that the shock thickness resolved in our approach is much smaller than the cell size of MHD simulations which are used to provide flow and magnetic fields for the calculation of particle acceleration in a similar way (e.g., [Kozarev et al. 2013](#); [Schwadron et al. 2015](#)).

The magnetic field is compressed when it is swept by the shock into the downstream region. In the shock layer (within $8 \delta_{sh}$), the magnetic field is determined by the MHD shock jump conditions in the local shock frame. The transverse component of the magnetic field with respect to the shock surface is given by $B_\Theta = B_{\Theta 0} V_{sh}/U(x')$, where $B_{\Theta 0}$ is the transverse component of the background field and x' is the distance to the shock front along the shock normal. The normal component of the magnetic field B_R remains unchanged. In the downstream region, the magnetic field is obtained from the ideal MHD induction equation ([Kong et al. 2017](#)). While our two-dimensional treatment is simplistic and leads to non-zero divergence of magnetic field at the shock front, we argue that particle acceleration and transport mainly depend on large-scale magnetic field geometry. However, we do acknowledge that the errors in magnetic field within the transition layer can mismatch parallel diffusion and perpendicular diffusion, and may influence our results. In the future three-dimensional studies, we will use more sophisticated treatment for ensuring the exact solution of Maxwell's equations (e.g., [Giacalone 2017](#)).

For diffusion coefficients used in the Parker transport equation, we first obtain particle diffusion both along and across the magnetic field for the reference run from a few considerations, and then vary them and see how the key results change. The diffusion coefficient tensor is given by,

$$\kappa_{ij} = \kappa_{\perp} \delta_{ij} + (\kappa_{\parallel} - \kappa_{\perp}) \frac{B_i B_j}{B^2}, \quad (2)$$

where κ_{\parallel} and κ_{\perp} are the parallel and perpendicular diffusion coefficients, and B_i is the average magnetic field vector. Note that the antisymmetric diffusion coefficient κ_A related to particle drifts is neglected here because the gradient and curvature drifts are out of the simulation plane. κ_{\parallel} can be calculated from the quasilinear theory (Jokipii 1971). We assume the magnetic turbulence is well developed and has a Kolmogorov power spectrum $P \propto k^{-5/3}$. When the particle gyroradius is much smaller than the correlation length of turbulence, the resulting diffusion coefficient $\kappa_{\parallel} \propto p^{4/3}$. The value of κ_{\parallel} has the following expression (Giacalone & Jokipii 1999),

$$\kappa_{\parallel} = \frac{3v^3}{20L_c\Omega^2\sigma^2} csc\left(\frac{3\pi}{5}\right) \left[1 + \frac{72}{7} \left(\frac{\Omega L_c}{v}\right)^{5/3}\right], \quad (3)$$

where v is the particle speed, L_c is the turbulence correlation length, σ^2 is the normalized wave variance of turbulence, and Ω is the particle gyrofrequency. The magnetic field and turbulence property in the corona is highly unknown as no in situ observation is available (see Zhao et al. (2018a) for latest observation of turbulence properties at 1 AU). For the reference run, we assume the average magnetic field in the simulation domain $B_0 = 1$ G, the turbulence correlation length $L_c = 0.01 R_{\odot}$, and the turbulence variance $\sigma^2 = \delta B^2/B_0^2 = 0.14$. The assumption of correlation length is similar to models of solar wind heating. For example, Hollweg (1986) assumed that the correlation length $L_c = 7520 (B/1 \text{ G})^{-1/2} \text{ km}$ ($\sim 0.01 R_{\odot}$ for $B_0 = 1$ G) based on the assumption that the correlation length is related to mean flux tube spacing, which in turn is related to the average field strength. Interplanetary observation of magnetic fluctuations suggests that the mean values of turbulence variance can be ~ 0.4 (e.g., Bavassano et al. 1982). Then, $\kappa_{\parallel 0} = 1.4 \times 10^{17} \text{ cm}^2 \text{ s}^{-1}$ for the proton initial energy $E_0 = 100$ keV. This value is similar to the choice found in previous works (e.g., Sokolov et al. 2004; Kocharov et al. 2012; Giacalone 2015).

In the simulations, we normalize the length $L_0 = 1 R_\odot = 7 \times 10^5$ km and the velocity $V_0 = V_{sh} = 2000$ km s⁻¹. So the normalization of the diffusion coefficient is $\kappa_0 = L_0 V_0 = 1.4 \times 10^{19}$ cm² s⁻¹, then $\kappa_{\parallel 0} = 0.01 \kappa_0$. We also consider $\kappa_{\parallel 0}/\kappa_0 = 0.1$ ($\sigma^2 = 0.014$) and 0.003 ($\sigma^2 = 0.4$) to examine the effect on particle acceleration. Test-particle simulations have suggested that the perpendicular diffusion coefficient κ_\perp is about a few percent (0.02-0.04) of the parallel diffusion coefficient κ_\parallel and their ratio $\kappa_\perp/\kappa_\parallel$ is nearly independent of particle energy (Giacalone & Jokipii 1999). We take $\kappa_\perp/\kappa_\parallel = 0.04$ in the reference run, and also consider $\kappa_\perp/\kappa_\parallel = 0.01$ and 0.003 to study its effect.

When the shock propagates outward, we inject protons with an initial energy $E_0 = 100$ keV continuously into the immediate region upstream of the shock at a constant rate. In each simulation, a total of 1.2×10^5 pseudo-particles are injected. We use a particle splitting technique to improve the statistics in the particle distribution at high energies (see, e.g., Giacalone & Jokipii 1996). For the reference run, at the end of the simulation, the total number of “daughter” particles with decreased weight is about six times more than the injected. The injection energy used here is roughly equal to what is required for the Parker transport equation to describe the acceleration process, i.e., the streaming anisotropy is small enough (Giacalone & Jokipii 1999). A particle will be removed from the simulation if it reaches the z -axis or hits the solar surface.

As mentioned above, to study the effect of various parameters on particle acceleration, such as the streamer tilt angle (Θ_{tilt}), particle spatial diffusion coefficient (by varying $\kappa_{\parallel 0}/\kappa_0$ and $\kappa_\perp/\kappa_\parallel$), and shock compression ratio (X), we do a parameter study by including eight simulations in addition to the reference run. A summary of the parameters that are varied in the simulations is listed in Table 1.

3. SIMULATION RESULTS

3.1. Results for Run 1

We first present the results for the reference simulation, i.e., Run 1 in Table 1. Figure 2 shows the spatial distributions of accelerated particles when the shock moves to three different heights, i.e., $2 R_\odot$ ($t = 245$ s), $3 R_\odot$ ($t = 595$ s), and $4 R_\odot$ ($t = 945$ s). Note that the shock heights in this

paper refer to that of the outermost shock front at the equator, which is $1.3 R_{\odot}$ in the beginning of the simulation ($t = 0$). The particles with relatively lower energies (10-30 p_0 , 10-90 MeV) are shown in the upper panels and with higher energies ($>30 p_0$, >90 MeV) are shown in the lower panels. Note that the associated animation shows the temporal evolution of particle distributions for three energy ranges, including the low-energy range <10 MeV not shown in the paper. The primary sources for particles with different energies are located at different regions and vary significantly as the shock propagates and expands. As shown in Figure 2, and the associated animation, relatively lower-energy (10-90 MeV) particles are initially accelerated at the upper flank of the shock in the open field region where the shock is perpendicular. Very few particles are accelerated to >90 MeV when the shock is still below $2 R_{\odot}$. Later, energetic particles begin to appear at the lower shock flank in the streamer region. As the shock moves to $3 R_{\odot}$, both 10-90 MeV and >90 MeV particles have the highest intensities in this region. This indicates that the streamer-like field plays a critical role for particles accelerated to above ~ 100 MeV, consistent with the results in our previous study (Kong et al. 2017). While the earlier study (Kong et al. 2017) has shown the shock-streamer interaction region can be a vital acceleration site for high-energy SEPs, the current simulation reveals a more complicated energetic particle distribution when the shock is propagating at a tilted angle compared to the streamer. For rest of the paper we will explore the consequence of this in more details.

For a planar shock with a compression ratio $X = 3$, the DSA theory predicts a power-law spectrum of particle distribution function $f(p) \propto p^{-3X/(X-1)} = p^{-4.5}$. Therefore, the particle differential intensity $dJ/dE = p^2 f(p) \sim E^{-1.25}$ for non-relativistic particles. Figure 3(a) shows the energy spectra of accelerated particles integrated over the whole simulation domain when the shock propagates to six different heights ranging from 1.5 to $4 R_{\odot}$. At low energies, the particle spectra are approximately a power law with a slope of -1.25 , agreeing well with the slope predicated by DSA theory. At high energies, the spectra break and roll over differently. Noticeably, the spectrum resembles a double power-law spectrum with a second power-law feature emerges in 10-100 MeV when the shock front arrives at $3-4 R_{\odot}$. We then fit the spectrum according to the Band function form (Band et al. 1993)

$$dJ/dE = CE^{-\gamma_1} \exp(-E/E_B) \quad \text{for } E \leq (\gamma_2 - \gamma_1)E_B,$$

$$= CE^{-\gamma_2}[(\gamma_2 - \gamma_1)E_B]^{\gamma_2 - \gamma_1} \exp(\gamma_1 - \gamma_2) \quad \text{for } E \geq (\gamma_2 - \gamma_1)E_B, \quad (4)$$

which has four parameters. Here C is the normalization constant, γ_1 and γ_2 are the power-law indices for low-energy and high-energy particles, and E_B is the break energy. The fitted spectrum to the particle spectrum at $3.5 R_\odot$ (blue line) with the double power law function is shown in Figure 3(b) as the dash-dotted line (multiplied by a factor of 10). The fitted parameters are $\gamma_1 = 1.25$, $\gamma_2 = 2.25$, $E_B = 20$ MeV, and $C = 3 \times 10^2$ (see also Figure 8(a)). Note that in this study we do not try to fit the spectrum in the whole energy range (e.g., the rapid rollover at the high-energy end), but give priority to a better fit to the low-energy portion. We will further discuss the emergence of double-power-law feature in particle spectra in Section 4.

As shown in Figure 3(a) and the associated animation, when the shock moves from 2.5 to $3 R_\odot$, the particle intensity around and above 100 MeV is enhanced dramatically. During this period, a nearly perpendicular shock geometry forms at the lower shock flank as the shock propagates through the streamer field, therefore resulting in much faster acceleration. In addition, the closed field lines of the streamer also contribute to efficient acceleration by trapping particles upstream of the shock. The configuration is similar to that occurring at the shock nose as shown in Kong et al. (2017).

We repeat the simulation of particle acceleration in a simple radial magnetic field as shown in Kong et al. (2017), and compare the particle spectra with Run 1 at three different shock heights in Figure 3(b). The particle spectra for the two simulations are overlapped below 10 MeV, approximately a power law with a slope of -1.25 . In the radial magnetic field, the particle spectra at different heights break around 10 MeV and roll over in a similar manner. In the streamer field case, the maximum energy achievable is much higher, and a significant amount of particles can be accelerated to >100 MeV. At 3 - $3.5 R_\odot$, the particle intensity at 100 MeV (200 MeV) is enhanced by more than one order (two orders) of magnitude in Run 1 compared to that in a radial field. Therefore, particle acceleration at a coronal shock propagating through the streamer-like field is much more efficient than that in a simple radial field. This indicates that the coronal magnetic field configuration can play an important role in producing large SEP events.

3.2. Effect of the streamer tilt angle

A CME-driven shock can interact with the streamer field at different shock heights depending on the shock speed and the distance between the CME eruption region and the streamer. Thus, the shock geometry and its temporal evolution in the shock-streamer interaction region can vary greatly for different events. Here we examine the effect of streamer tilt angle (Θ_{tilt}) on particle acceleration by considering other two cases, i.e., the streamer field rotated by 30° and 60° . A comparison of particle spectra for the three simulations, Runs 1, 2, and 3 in Table 1, is shown in Figure 4. At low shock heights, there are no significant difference. At the shock propagates outward, a rapid hardening in particle spectrum above tens of MeV occurs between 2-2.5 R_\odot in Run 2, between 2.5-3 R_\odot in Run 1, and between 3-3.5 R_\odot in Run 3. This is because the configuration favorable for rapid acceleration of particles start to form later when Θ_{tilt} is larger.

We fit the particle spectra at 3.5 R_\odot (blue lines) for the three runs with a double power law function, as denoted by black dot-dashed lines (see also Figure 8(a), (b), (c)). The break energy decreases as increasing Θ_{tilt} from 30° to 60° , being 25 MeV, 20 MeV, and 13 MeV, for Runs 2, 1, and 3, respectively. The high-energy power law slope is similar for Runs 1 and 2 ($\gamma_2 = 2.25$), but is slightly steeper for Run 3 ($\gamma_2 = 2.4$).

3.3. Effect of the value of diffusion coefficient

The diffusion coefficient describes how well the particles are confined near the shock, therefore has a critical effect on the particle acceleration rate. The characteristic time for particles to be accelerated from p_0 to p at a planar shock is given by (e.g., [Drury 1983](#)),

$$\tau_A = \frac{3}{U_1 - U_2} \int_{p_0}^p \frac{dp'}{p'} \left(\frac{\kappa_{xx,1}(p')}{U_{x,1}} + \frac{\kappa_{xx,2}(p')}{U_{x,2}} \right), \quad (5)$$

where the subscripts x and xx refer to the direction normal to the shock, 1 and 2 the upstream and downstream regions of the shock. Thus, for a smaller diffusion coefficient, the acceleration time is shorter, and the maximum energy attainable will be larger.

We examine the effect of the value of diffusion coefficient by adopting different values of $\kappa_{\parallel 0}/\kappa_0$ and keeping the same ratio $\kappa_{\perp}/\kappa_{\parallel}$. Figure 5 shows the temporal evolution of particle spectra for Runs

1, 4, and 5, with $\kappa_{\parallel 0}/\kappa_0$ being 0.01, 0.1, and 0.003, respectively. Note that for clarity we only plot particle spectra at three shock heights because the spectral slopes vary greatly for different values of $\kappa_{\parallel 0}/\kappa_0$. As expected, when the diffusion coefficient is smaller, the particle spectrum is significantly harder. At $3.5 R_{\odot}$, the particle intensity at 100 MeV is enhanced by nearly one order of magnitude for Run 5 compared to Run 1, while the maximum energy in Run 4 is only ~ 30 MeV.

Same as Figure 4, the fittings of particle spectra at $3.5 R_{\odot}$ (blue lines) for the three runs with a double power law function are denoted by black dot-dashed lines (see also Figure 8(a), (d), (e)). The break energy E_B increases when $\kappa_{\parallel 0}/\kappa_0$ is smaller, being 0.8 MeV, 20 MeV, and 90 MeV, for Runs 4, 1, and 5, respectively. The second power law extends to ~ 700 MeV in Run 5 ($\kappa_{\parallel 0}/\kappa_0 = 0.003$), compared to only ~ 10 MeV in Run 4 ($\kappa_{\parallel 0}/\kappa_0 = 0.1$).

3.4. *Effect of the value of perpendicular diffusion*

Perpendicular diffusion plays an important role in particle acceleration at quasi-perpendicular shocks and longitudinal transport of SEPs. Generally charged particles tend to move following individual field lines. The diffusion of particles perpendicular to the mean magnetic field includes two forms, the actual crossing of field lines due to scattering or drift and random walking along meandering field lines. Previous test-particle calculations give a perpendicular diffusion coefficient of about a few percent of the parallel diffusion and nearly independent of particle energy (Giacalone & Jokipii 1999). Here we examine the effect of perpendicular diffusion by adopting three different values of $\kappa_{\perp}/\kappa_{\parallel}$, being 0.04, 0.01, and 0.003, in Runs 1, 6, and 7, respectively.

Figure 6 shows the temporal evolution of particle spectra for the three cases. The high energy portion of the spectra rolls over more slowly in Runs 6 and 7 than in Run 1. This indicates that the maximum energy of particles is much higher when $\kappa_{\perp}/\kappa_{\parallel}$ is smaller. We fit the particle spectra at $3.5 R_{\odot}$ (blue lines) for the three runs with a double power law function, as denoted by black dot-dashed lines (see also Figure 8(a), (f), (g)). The break energy ($E_B = 20$ MeV) and the high-energy spectral slope ($\gamma_2 = 2.25$) do not vary with $\kappa_{\perp}/\kappa_{\parallel}$, but the high-energy power law extends to much higher energies, ~ 400 MeV in Run 6 and ~ 1 GeV in Run 7, compared to ~ 100 MeV in Run 1.

3.5. *Effect of the shock compression ratio*

It is known that strong shocks are more rapid accelerators of particles than weak shocks. In the DSA theory, the power law slope of particle distribution function only depends on the compression ratio (X) when applied to a planar shock, i.e., $\alpha = -3X/(X - 1)$. The particle spectrum is steeper for smaller X . Recent observations have shown that the density compression ratio along the shock front is in the wide range of 1 to 3 (e.g., [Bemporad & Mancuso 2010](#); [Bemporad et al. 2014](#); [Susino et al. 2015](#)). We examine the effect of the compression ratio by considering three different values of X , being 3, 2.5, and 2 in Runs 1, 8, and 9, respectively.

Figure 7 shows the temporal evolution of particle spectra for the three cases. As expected, the particle spectra in Runs 8 and 9 drop more steeply at high energies than in Run 1. The particle intensity around 100 MeV is declined by nearly one order (two orders) of magnitude in Run 8 (Run 9). We fit the particle spectra at $3.5 R_{\odot}$ (blue lines) for the three runs with a double power law function, as denoted by black dot-dashed lines (see also Figure 8(a), (h), (i)). The break energy E_B decreases when X is smaller, being 20 MeV, 15 MeV, and 7 MeV, in Runs 1, 8, and 9, respectively. Both the low-energy and high-energy power law slopes get steeper. γ_1 increases from 1.25 to 1.5 and 2, and γ_2 increases from 2.25 to 2.5 and 2.8.

4. DISCUSSION ON THE DOUBLE-POWER-LAW FEATURE IN PARTICLE ENERGY SPECTRA

In many large SEP or GLE events, the particle energy spectra exhibit spectral breaks or rollovers at high energies. It was also shown that the break energies depend on the ion charge-to-mass ratio ([Cohen et al. 2005](#); [Mewaldt et al. 2005](#); [Desai et al. 2016b](#)). The broken spectra are usually described either by a power law with exponential rollover ([Ellison & Ramaty 1985](#)) or a double power law ([Band et al. 1993](#)). [Mewaldt et al. \(2012\)](#) analyzed 16 GLE events in solar cycle 23 and found that the proton spectra show spectral breaks at energies ranging from ~ 2 to ~ 46 MeV and can be well fitted by a double power law up to ~ 500 - 700 MeV (see also, [Desai et al. 2016a,b](#); [Wu & Qin 2018](#)). [Cohen & Mewaldt \(2018\)](#) also found that the particle spectra for proton and other ions in the 2017 September

10 GLE event can be fitted with double power laws and show similar spectral indices (except for proton). However, Bruno et al. (2018) showed that the particle spectra between ~ 80 MeV and a few GeV in 26 major SEP events observed by PAMELA are well described by a power law with exponential rollover, with a spectral slope of 2.2 and break energy at ~ 170 MeV on average.

The steady-state DSA predicts a power law spectrum for a planar shock. However, the physical mechanism responsible for producing spectral breaks, particularly the double power law spectra, is unclear. Spectral breaks may occur due to effects such as finite acceleration time, finite shock size, shock geometry, and adiabatic cooling (e.g., Zank et al. 2000; Li et al. 2005; Tylka et al. 2005; Tylka & Lee 2006; Li et al. 2009; Schwadron et al. 2015; Zhao et al. 2016a,b). Li et al. (2005) found that a broken power law solution can be achieved if an extra loss term is included in the standard DSA solution. Schwadron et al. (2015) obtained broken power-law solutions when considering injection of seed particles in a fixed length along the shock. By assuming a single power-law near the Sun, Zhao et al. (2016b) reproduced the double power law spectrum at 1 AU, as a result of pitch-angle diffusion by magnetic turbulence during particle transport in interplanetary space (see also, Li & Lee 2015).

In our numerical model, the acceleration rate varies considerably along the shock front as it sweeping through different magnetic fields. To understand the origin of double-power-law features in the simulations, we divide the whole simulation domain into two regions, i.e., the streamer region and non-streamer region, as shown by the black dashed line in Figure 2(d). The line is set to be at $\Theta = -40^\circ$ (-30°) for runs with streamer tilt angles of 45° and 60° (30°). It can roughly separate the particles accelerated mainly in the two regions, but at later time particles from the two regions may be mixed together due to cross-field diffusion, as shown in Figure 2.

Figure 8 shows the particle spectra when the shock moves to $3.5 R_\odot$ for all simulations. The spectrum integrated for all particles over the whole domain is plotted by the blue line, while the spectra in streamer and non-streamer regions are plotted by thin red and green lines, respectively. In all cases, the particle spectra from streamer regions have much higher rollover energies, but relatively lower intensity in low energy ranges. That is, the low-energy spectra are dominated by particles from non-streamer region, while the high-energy spectra are dominated by particles from streamer regions.

We fit all the integrated spectra (blue lines) with a double power law function, as denoted by the black dotted lines. It implies that the combination of two particle spectra ordered like these can readily produce a double power law feature in the combined spectra. In observations, the event-integrated SEP spectra obtained at 1 AU may sample energetic particles accelerated at different locations along the shock due to cross-field diffusion or even from different CME-driven shocks, therefore the double power laws observed in large SEP events may also be affected by the mixing of SEPs from different source regions.

5. CONCLUSIONS

In this study, we have further investigated the effect of large-scale coronal magnetic configuration on particle acceleration at coronal shocks. The shock is represented by an expanding circular front and the coronal magnetic field is given by an analytical solution of a streamer-like configuration (Kong et al. 2017). The acceleration of particles at the shock is modelled by numerically solving the Parker transport equation through a stochastic integration method. We consider a CME-driven shock originates outside of the streamer and propagates through the streamer from the flank. We also conduct a parameter study to examine the effect of various parameters on particle acceleration at coronal shocks, such as the streamer tilt angle, particle spatial diffusion coefficient, and shock compression ratio.

Our calculations show that the primary acceleration regions differ significantly for particles with different energies and vary as the shock propagates. For example, 10-90 MeV particles are initially accelerated at the upper shock flank in the open field and later begin to appear at the lower shock flank in the streamer region, while >100 MeV particles are mainly accelerated in the shock-streamer interaction region. A comparison of the particle spectra to that in a radial magnetic field shows that the particle intensity at 100 MeV (200 MeV) is enhanced by more than one order (two orders) of magnitude in the streamer field. This indicates that the streamer-like magnetic field can be an important factor in producing large SEP events, consistent with the results in Kong et al. (2017). In addition, the particle spectra at $3-4 R_{\odot}$ can be well fitted with a double power law up to ~ 100 MeV. At energies below ~ 10 MeV, the spectra are a power law with a slope of -1.25 , agreeing well

with the slope predicated by DSA theory. At higher energies up to ~ 100 MeV, a second power law emerges, with a slope of about -2.25 . The break energy E_B is around 20 MeV.

Our calculations also show that the particle spectra are affected considerably by a number of parameters. When the streamer tilt angle Θ_{tilt} increases from 30° to 60° , the break energy E_B declines from 25 MeV to 13 MeV, and the high energy power law slope is steeper, with γ_2 varying from 2.25 to 2.4. When the diffusion coefficient is smaller by reducing $\kappa_{||0}/\kappa_0$ from 0.1 to 0.003, the particle spectrum gets significantly harder, with E_B increasing from 0.8 MeV to 90 MeV, and the high-energy end of the second power law extending from ~ 10 MeV to ~ 700 MeV. When the perpendicular diffusion is smaller by reducing the ratio $\kappa_{\perp}/\kappa_{||}$ from 0.04 to 0.003, E_B and γ_2 do not change, but the high-energy power law can extend to ~ 1 GeV. When the shock is weaker by reducing X from 3 to 2, the particle spectra drop more steeply at high energies, with E_B decreasing to 7 MeV, and γ_1 and γ_2 increasing to 2 and 2.8, respectively.

The physical mechanisms for double power laws observed in many large SEP or GLE events remain unclear. Our study shows that a double power law feature emerges readily in particle spectra during acceleration at coronal shocks. Further analysis suggests that it may be a mixture of two distinct populations accelerated mainly in the streamer and open field regions, where the particle acceleration rate differs substantially. Because the event-integrated spectra observed at 1 AU can sample SEPs from different shock regions or sources due to cross-field diffusion, the mixing effect may also contribute to the formation of double power laws at 1 AU. It is known that the SEP spectra observed at 1 AU are smeared during interplanetary transport, due to effects such as pitch angle scattering and mixing of different sources. The recently launched Parker Solar Probe (PSP) will provide observations close to the particle acceleration site near the Sun and help improve our understanding of the acceleration and transport of SEPs and the formation of spectral breaks (Desai & Giacalone 2016). A clear prediction from the current study is that PSP may observe energetic particles from individual source regions before they are mixed together.

The shock-streamer interaction configuration in this work may also have important implications for sustained γ -ray emission (SGRE) events, in which γ -ray emission above 100 MeV can last for hours

after the flare impulsive phase (see, e.g., [Kahler et al. 2018](#); [Klein et al. 2018](#); [Share et al. 2018](#), and references therein). The >100 MeV γ -ray emission is thought to be produced by the decay of pions from interactions of >300 MeV protons with background ions in the solar atmosphere. About 30 SGRE events have been observed by *Fermi* since its launch in 2008, including the two GLE events in this solar cycle. SGRE events pose a challenge to models of particle acceleration and transport. Most of latest works favor the CME-driven shock acceleration as the source of high-energy protons, but how the accelerated particles precipitate to the solar photosphere to produce the prolonged γ -ray emission remain elusive. As shown in our study, the shock-streamer interaction configuration can provide both efficient acceleration and trapping of energetic particles due to closed field lines of streamers ([Hudson 2018](#); [Kahler et al. 2018](#)). Future work will focus on the transport of high-energy protons accelerated by the CME-driven shocks and implications for SGRE events.

We thank Dr. Mihir Desai for useful comments. This work was supported by the National Natural Science Foundation of China (under grants 11873036, 11503014 and 11790304 (11790300)), the Young Elite Scientists Sponsorship Program by China Association for Science and Technology, the Young Scholars Program of Shandong University, Weihai, and the Project Supported by the Specialized Research Fund for State Key Laboratories. F.G. acknowledges the support from the National Science Foundation under grant 1735414 and support from by the U.S. Department of Energy, Office of Science, Office of Fusion Energy Science, under Award Number DE-SC0018240. The work of J.G. was supported by NSF under grant 1735422. The work was carried out at National Supercomputer Center in Tianjin, and the calculations were performed on TianHe-1(A). We acknowledge the use of GONG magnetic synoptic maps, SOHO LASCO and STEREO SECCHI coronagraph images.

APPENDIX

A. OBSERVATIONS

The two GLE events in solar cycle 24 occurred on 2012 May 17 and 2017 September 10, respectively. Figure 9 shows the *GONG* synoptic magnetic magnetograms and coronal magnetic field by the Potential Field Source Surface (PFSS) model for the two events (<https://gong.nso.edu/data/>

[magma](#)). The yellow arrows point to the active regions (ARs) of two CMEs, i.e., AR 11476 and AR 12673. The streamer belt is illustrated by the tallest closed field lines meandering around the circumference of the Sun in blue in panels (b) and (d). In the first event the CME originated below the streamer belt ([Rouillard et al. 2016](#)), while in the second event the CME eruption region is located outside and near the edge of the streamer belt ([Luhmann et al. 2018](#)).

Figure 10 shows white-light coronagraph observations of the interaction between CME-shock and streamers for the GLE event on 2017 September 10. The AR12673 is located at the west limb as seen from near-Earth orbit, e.g., in field of view (FOV) SOHO/LASCO. During this event, the separation angle of STEREO Ahead (STA) with Earth is $\sim 128^\circ$, therefore in STA FOV the AR is located behind the east limb. In panel (a) at 16:00 UT the CME first appeared in the FOV of STA/COR1, and in panel (b) at 16:05 UT the streamers have been strongly deflected by the CME flanks. Later, in panels (c) and (d), the outermost CME front shows a bubble-shaped structure in the FOVs of both STA/COR2 and SOHO/LASCO/C2. As shown in [Kwon et al. \(2014\)](#), the outermost faint CME front represents a fast magnetosonic shock wave and can be well reproduced with the ellipsoid model. The CME-driven shock propagated freely ahead of the CME ejecta, and strongly deflected and passed through the surrounding streamers.

REFERENCES

- | | |
|--|---|
| Band, D., Matteson, J., Ford, L., et al. 1993, <i>ApJ</i> , 413, 281 | Cane, H. V., Reames, D. V., & von Rosenvinge, T. T. 1988, <i>JGR</i> , 93, 9555 |
| Bavassano, B., Dobrowolny, M., Fanfoni, G., et al. 1982, <i>SoPh</i> , 78, 373 | Chen, Y., Du, G. H., Feng, L., et al. 2014, <i>ApJ</i> , 787, 59 |
| Bemporad, A., & Mancuso, S. 2010, <i>ApJ</i> , 720, 130 | Chen, Y., Song, H. Q., Li, B., et al. 2010, <i>ApJ</i> , 714, 644 |
| Bemporad, A., Susino, R., Lapenta, G. 2014, <i>ApJ</i> , 784, 102 | Cho, K. S., Bong, S. C., Kim, Y. H., et al. 2008, <i>A&A</i> , 491, 873 |
| Bruno, A., Bazilevskaya G. A., Boezio, M., et al. 2018, <i>ApJ</i> , 862, 97 | Cho, K.-S., Gopalswamy, N., Kwon, R.-Y., et al. 2013, <i>ApJ</i> , 765, 148 |

- Cohen, C. M. S., & Mewaldt, R. A. 2018, *Space Weather*, 16
- Cohen, C. M. S., Stone, E., Mewaldt, R. A., et al. 2005, *JGR*, 110, A09
- Desai, M. I., & Giacalone, J. 2016, *LRSP*, 13, 3
- Desai, M. I., Mason, G. M., Dayeh, M. A., et al. 2016, *ApJa*, 816, 68
- Desai, M. I., Mason, G. M., Dayeh, M. A., et al. 2016, *ApJb*, 828, 106
- Drury, L. O. 1983, *Rep. Prog. Phys.* 46, 973
- Ellison, D. C., & Ramaty, R. 1985, *ApJ*, 298, 400
- Feng, S. W., Chen, Y., Kong, X. L., et al. 2012, *ApJ*, 753, 21
- Feng, S. W., Chen, Y., Kong, X. L., et al. 2013, *ApJ*, 767, 29
- Feng, S. W., Chen, Y., Li, B., et al. 2011, *SoPh*, 272, 119
- Giacalone, J. 2005a, *ApJ*, 624, 765
- Giacalone, J. 2005b, *ApJ*, 628, L37
- Giacalone, J. 2015, *ApJ*, 799, 80
- Giacalone, J. 2017, *ApJ*, 848, 123
- Giacalone, J., & Jokipii, J. R. 1996, *JGR*, 101, 11095
- Giacalone, J., & Jokipii, J. R. 1999, *ApJ*, 520, 204
- Gopalswamy, N., Xie, H., Akiyama, S., et al. 2013a, *ApJL*, 765, L30
- Gopalswamy, N., Xie, H., Akiyama, S., et al. 2014, *EP&S*, 66, 104
- Gopalswamy, N., Xie, H., Makela, P., et al. 2013b, *AdSpR*, 51, 1981
- Gopalswamy, N., Xie, H., Yashiro, S., et al. 2012, *SSRv*, 171, 23
- Gopalswamy, N., Yashiro, S., Makela, P. et al. 2018, *ApJL*, 863, L39
- Guo, J., Dumbovic, M., Wimmer-Schweingruber, R. F., et al. 2018, *SpWea*, 16, 1156
- Guo, F., Jokipii, J. R., & Kota, J. 2010, *ApJ*, 725, 128
- Guo, F., & Giacalone, J. 2013, *ApJ*, 773, 158
- Hollweg, J. V. 1986, *JGR*, 91, 4111
- Hudson, H. S. 2018, in *IAU Symp.* 335, *Space Weather of the Heliosphere: Processes and Forecasts*, ed. C. Foullon & O. Malandraki (Cambridge: Cambridge Univ. Press), 49
- Jokipii, J. R. 1971, *Rev. Geophys.*, 9, 27
- Jokipii, J. R. 1987, *ApJ*, 313, 842
- Kahler, S. W. 2005, *JGR*, 110, A12
- Kahler, S. W. 2016, *ApJ*, 819, 105
- Kahler, S. W., Cliver, E. W., Kazachenko, M. 2018, *ApJ*, 868, 81
- Kahler, S. W., Reames, D. V., & Burkepile, J. T. 2000, in *ASP Conf. Ser.* 206, *High Energy Solar Physics Workshop*, ed. R. Ramaty & N. Mandzhavidze (San Francisco, CA: ASP), 468
- Klein, K.-L., Tziotziou, K., Zucca, P., et al. 2018, *ASSL*, 444, 133
- Kozarev, K., Evans, R. M., Schwadron, N. A., et al. 2013, *ApJ*, 778, 43
- Kocharov, L., Pohjolainen, S., Mishev, A., et al. 2017, *ApJ*, 839, 79
- Kocharov, L., Vainio, R., Pomoell, J., et al. 2012, *ApJ*, 753, 87
- Kong, X. L., Chen, Y., Guo, F., et al. 2015, *ApJ*, 798, 81

- Kong, X. L., Chen, Y., Guo, F., et al. 2016, *ApJ*, 821, 32
- Kong, X. L., Chen, Y., Li, G., et al. 2012, *ApJ*, 750, 158
- Kong, X. L., Guo, F., Giacalone, J., Li, H., Chen, Y. 2017, *ApJ*, 851, 38
- Kwon, R.-Y., Zhang, J., & Olmedo, O. 2014, *ApJ*, 794, 148
- Kwon, R.-Y., & Vourlidas, A. 2018, *JSWSC*, 8, A08
- Kumar, P., Innes, D. E., & Cho, K. S. 2016, *ApJ*, 828, 28
- Lario, D., Kwon, R.-Y., Richardson, I. G., et al. 2017, *ApJ*, 838, 51
- Li, X., Guo, F., Li, H., & Li, S. 2018, *ApJ*, 866, 4
- Li, G., & Lee, M. A. 2015, *ApJ*, 810, 82
- Li, G., Hu, Q., & Zank, G. P. 2005, in *AIP Conf. Proc.* 781, *The Physics of Collisionless Shocks*, ed. G. Li, G. P. Zank, & C. T. Russell (Melville, NY:AIP), 233
- Li, G., Zank, G. P., Verkhoglyadova, O. P., et al. 2009, *ApJ*, 702, 998
- Liu, Y. D., Zhu, B., Zhao, X. 2019, *ApJ*, 871, 8
- Luhmann, J. G., Mays, M. L., Li, Y., et al. 2018, *SpWea*, 16, 557
- Low, B. C. 1986, *ApJ*, 310, 953
- Ma, S., Raymond, J., Golub, L., et al. 2011, *ApJ*, 738, 160
- Mancuso, S., & Raymond, J. C. 2004, *A&A*, 413, 363
- Mewaldt, R. A., Cohen, C. M. S., Labrador, A. W., et al. 2005, *JGR*, 110, A09S18
- Mewaldt, R. A., Cohen, C., Mason, G., et al. 2015, *Proc. 34th ICRC*, 30
- Mewaldt, R. A., Looper, M. D., Cohen, C. M. S., et al. 2012, *SSRv*, 171, 97
- Nelson, G. J., & Melrose, D. B. 1985, in *Solar Radiophysics*, ed. D. J. McLean & N. R. Labrum (Cambridge: Cambridge Univ. Press), 333
- Parker, E. N. 1965, *Planet. Space Sci.*, 13, 9
- Pohjolainen, S., Pomoell, J., & Vainio, R. 2008, *A&A*, 490, 357
- Reames D. V., Kahler S. W., & Ng C. K. 1997, *ApJ*, 491, 414
- Reames, D. V. 1999, *SSRv*, 90, 413
- Reames, D. V. 2009a, *ApJ*, 693, 812
- Reames, D. V. 2009b, *ApJ*, 706, 844
- Reiner, M. J., Vourlidas, A., Cyr, O. C. St., et al. 2003, *ApJ*, 590, 533
- Rouillard, A. P., Plotnikov, I., Pinto, R. F., et al. 2016, *ApJ*, 833, 45
- Schwadron, N. A., Lee, M. A., Gorby, M., et al. 2015, *ApJ*, 810, 97
- Senanayake, U. K., & Florinski, V. 2013, *ApJ*, 778, 122
- Share, G. H., Murphy, R. J., White, S. M., et al. 2018, *ApJ*, 869, 182
- Shen, C., Li, G., Kong, X., et al. 2013, *ApJ*, 763, 114
- Sokolov, I. V., Roussev, I. I., Gombosi, T. I., et al. 2004, *ApJL*, 616, L171
- Susino, R., Bemporad, A., Mancuso, S. 2015, *ApJ*, 812, 119

- Tylka, A. J., Cohen, C. M. S., Dietrich, W. F., et al. 2005, *ApJ*, 625, 474
- Tylka, A. J., & Lee, M. A. 2006, *ApJ*, 646, 1319
- Vainio, R., Raukunen, O., Tylka, A., et al. 2017, *A&A*, 604, A47
- Verkhoglyadova, O. P., Zank, G. P., & Li, G. 2015, *PhR*, 557, 1
- Wu, S. S., & Qin, G. 2018, *JGR*, 123
- Zank, G. P., Rice, W. K. M., & Wu, C. C. 2000, *JGR*, 105, 25079
- Zhao, L., Li, G., Mason, G. M., et al. 2016a, *RAA*, 16, 190
- Zhao, L., Zhang, M., & Rassoul, H. K. 2016b, *ApJ*, 821, 62
- Zhao, L. L., Adhikari, L., Zank, G. P., et al. 2018a, *ApJ*, 856, 94
- Zhao, M. X., Le, G. M., & Chi, Y. T. 2018b, *RAA*, 18, 74

Table 1. Parameters for all simulations

Run	Θ_{tilt}	$\kappa_{ 0}/\kappa_0$	$\kappa_{\perp}/\kappa_{ }$	X
1	45°	0.01	0.04	3
2	30°	0.01	0.04	3
3	60°	0.01	0.04	3
4	45°	0.1	0.04	3
5	45°	0.003	0.04	3
6	45°	0.01	0.01	3
7	45°	0.01	0.003	3
8	45°	0.01	0.04	2.5
9	45°	0.01	0.04	2

NOTE—In all simulations, the shock speed $V_{sh} = 2000 \text{ km s}^{-1}$, and the diffusion coefficient has a momentum dependence, $\kappa_{||} = \kappa_{||0}(p/p_0)^{4/3}$.

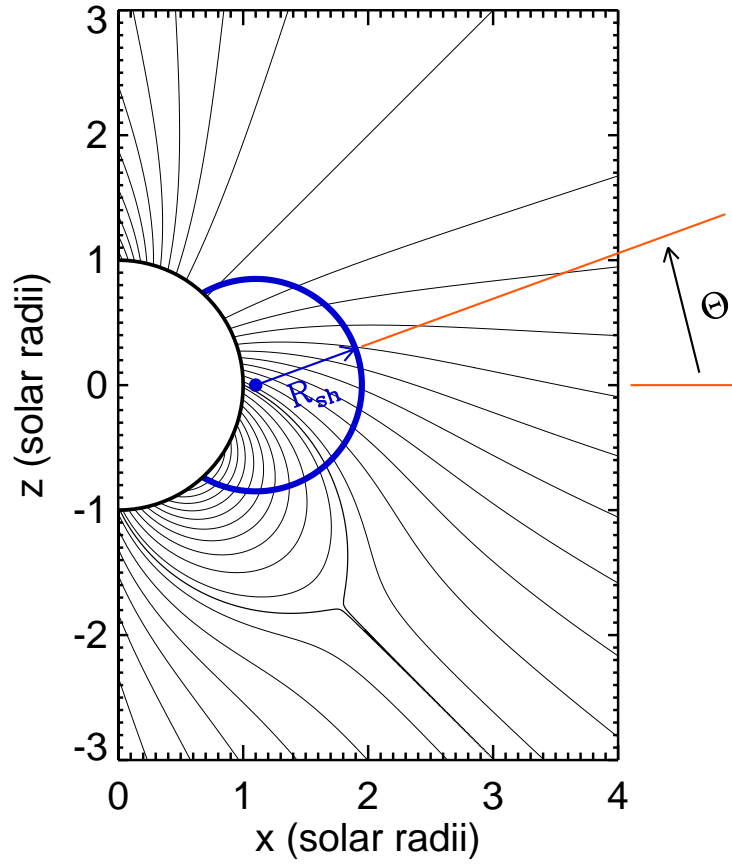


Figure 1. Schematics of the coronal shock morphology (thick blue circle) and the streamer-like coronal magnetic field (black lines). The blue dot indicates the center of the shock, fixed at $0.1 R_{\odot}$ above the solar surface.

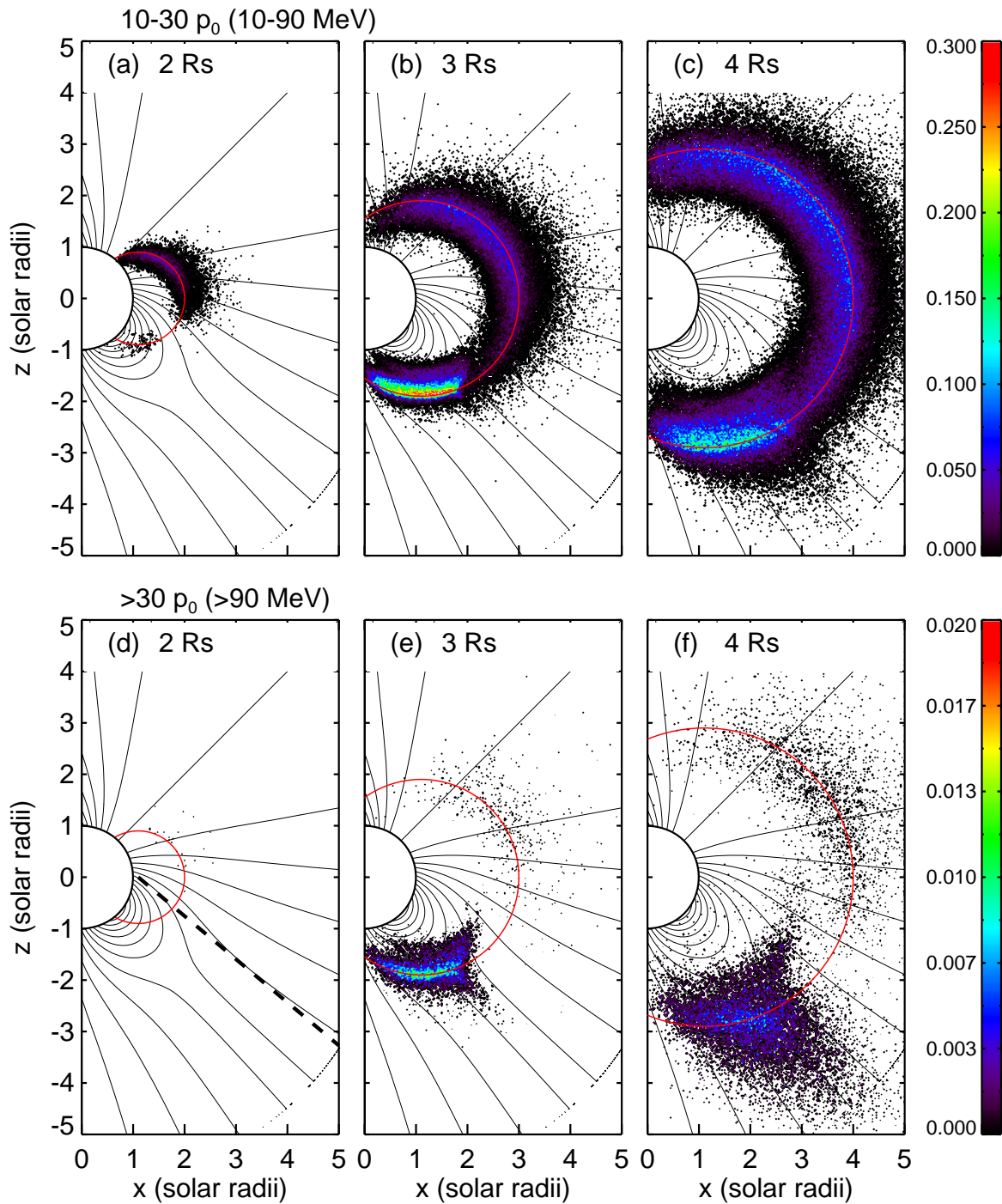


Figure 2. Spatial distributions of accelerated particles with energies 10-90 MeV (upper panels) and >90 MeV (lower panels), when the shock reaches three different heights, i.e., $2 R_\odot$, $3 R_\odot$, and $4 R_\odot$, for Run 1. The shock front is denoted by the red circle in each panel. Note that the shock heights in the figures refer to that of the outermost shock front in x direction. (An animation of this figure is available.)

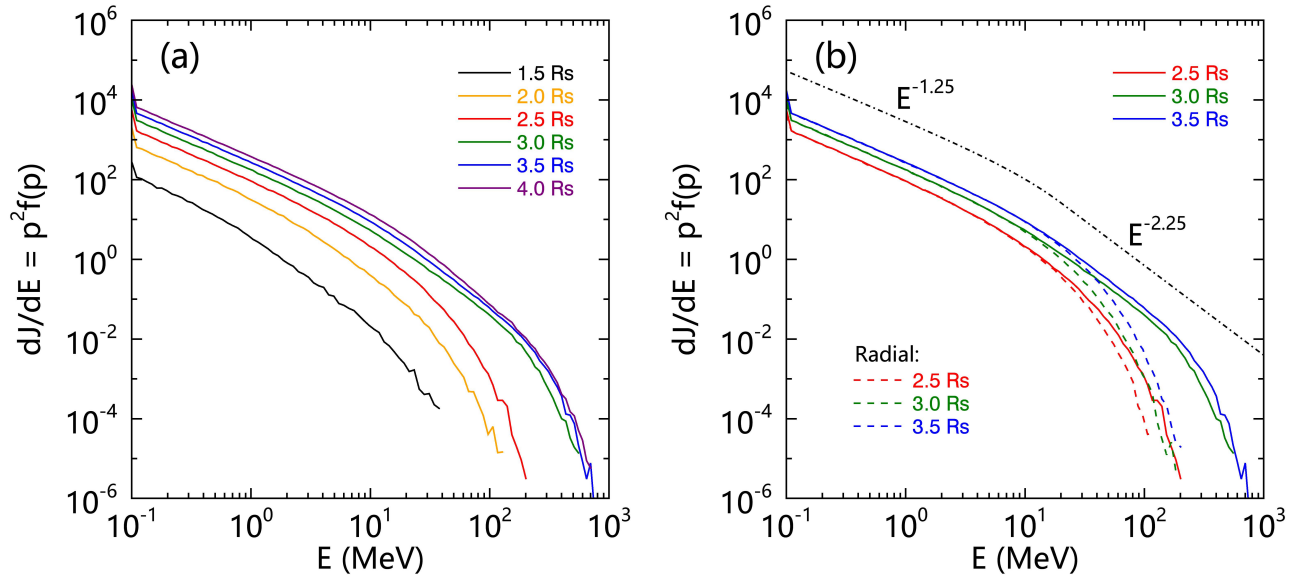


Figure 3. (a) Energy spectra of accelerated particles when the shock propagates to different heights for Run 1. (b) Comparison of particle spectra of Run 1 with that in a radial magnetic field. The black dash-dotted line illustrates the fitting of particle spectrum at $3.5 R_\odot$ (solid blue line) with a double power law function (multiplied by a factor of 10).

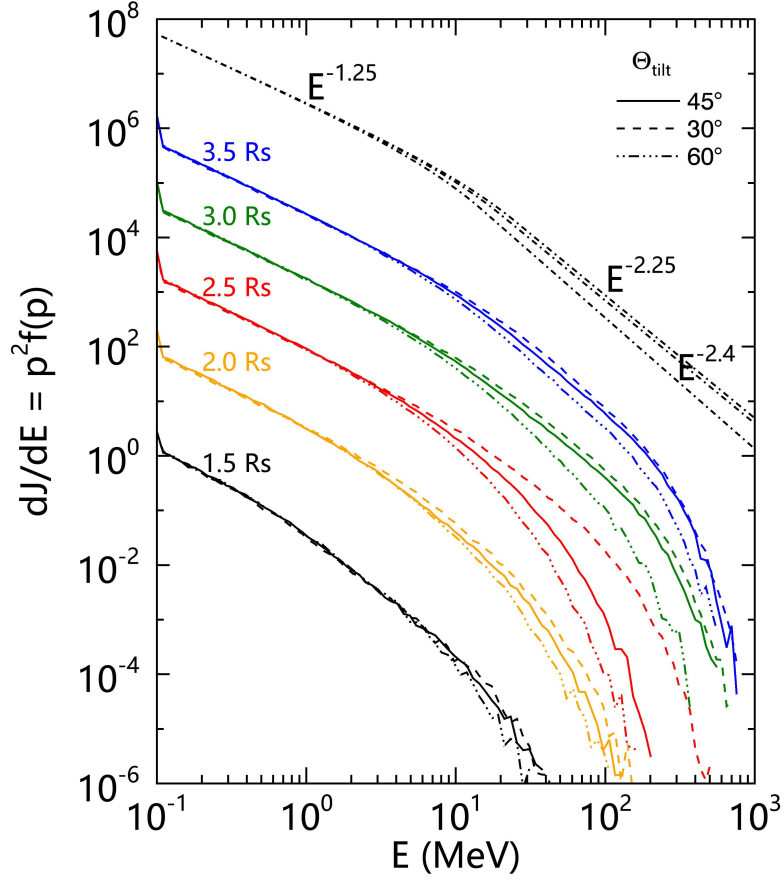


Figure 4. Energy spectra of accelerated particles when the shock propagates to different heights for Runs 1, 2, and 3, with different streamer tilt angles ($\Theta_{\text{tilt}} = 45^\circ, 30^\circ, \text{ and } 60^\circ$). The spectral profiles at different heights are multiplied by factors of 0.01, 0.1, 1, 10, and 100, respectively. The black dash-dotted lines indicate the fitting of particle spectra at $3.5 R_\odot$ (blue lines) with a double power law function (multiplied by a factor of 100).

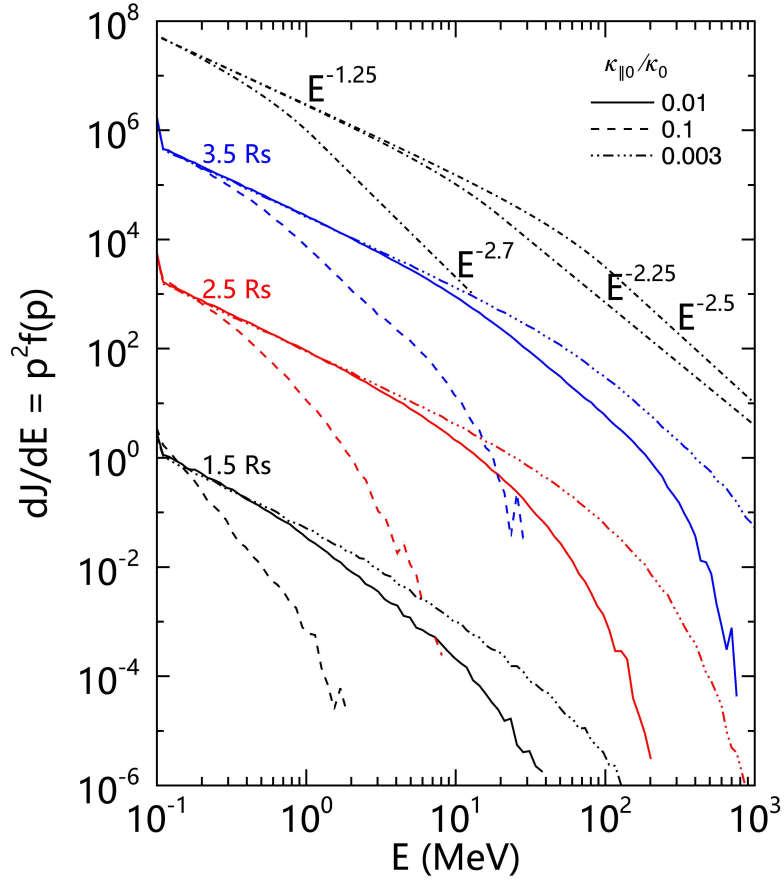


Figure 5. Same as Figure 4, but plotted for Runs 1, 4, and 5 with three different values of $\kappa_{\parallel 0}/\kappa_0$ ($= 0.01$, 0.1 , and 0.003).

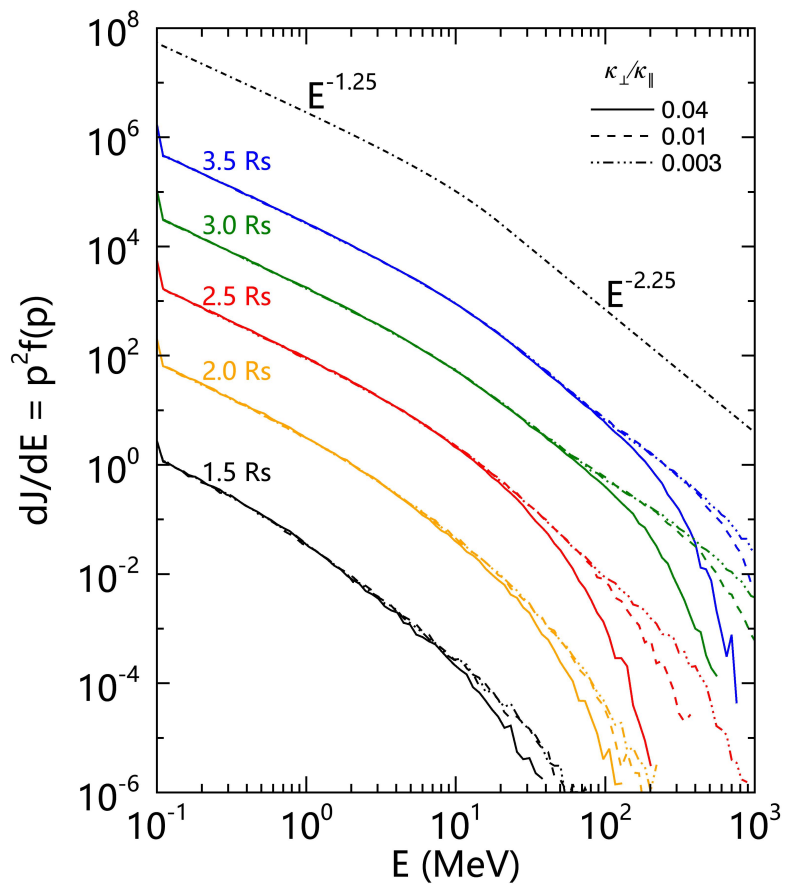


Figure 6. Same as Figure 4, but plotted for Runs 1, 6, and 7 with three different values of $\kappa_{\perp}/\kappa_{\parallel}$ ($= 0.04$, 0.01 , and 0.003).

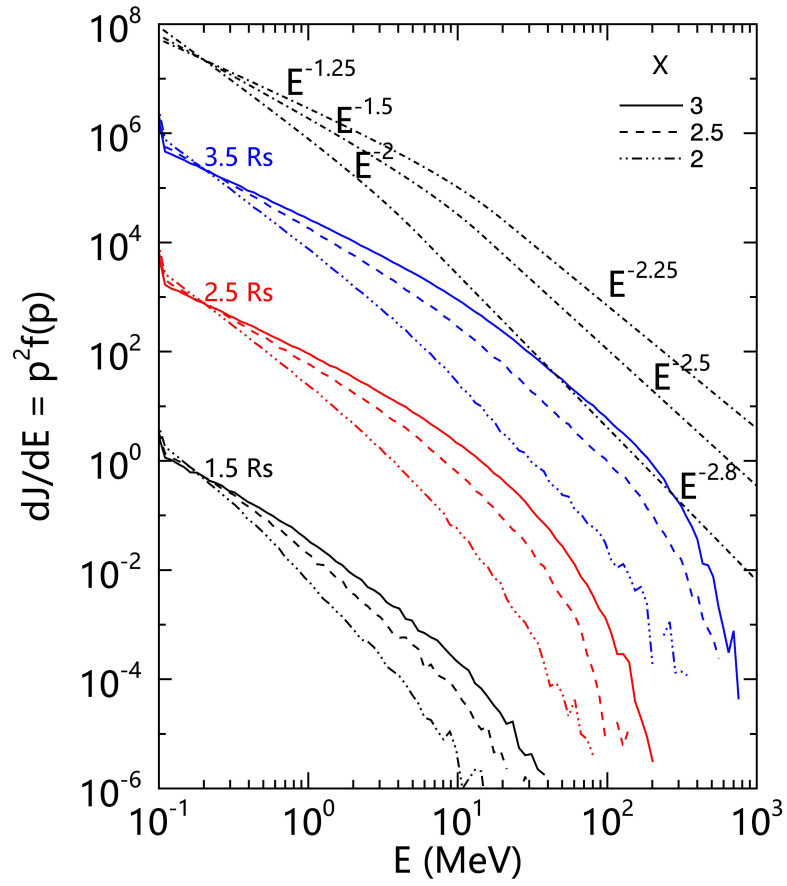


Figure 7. Same as Figure 4, but plotted for Runs 1, 8, and 9 with three different shock compression ratios ($X = 3, 2.5, 2$).

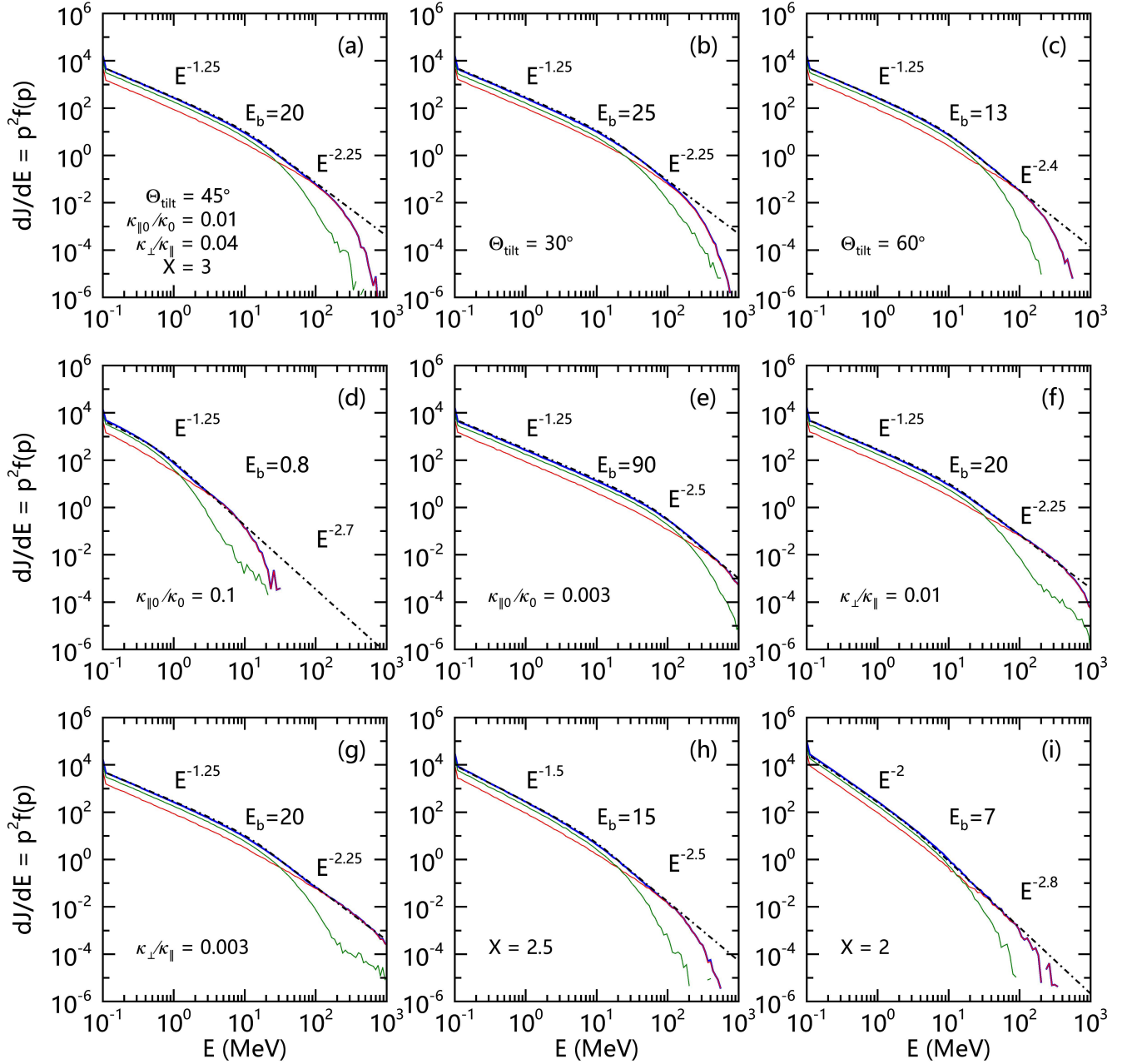


Figure 8. Particle energy spectra when the shock reaches $3.5 R_{\odot}$ for all simulations. The parameter that is changed in each simulation compared to that of Run 1 in panel (a) is denoted. The blue line shows the spectra integrated over the whole simulation domain, while the thin red and green lines show the separated spectra of the streamer region and outside-of-streamer region, as divided by the black dashed line in Figure 2. The integrated spectrum (blue line) in each simulation is fitted with a double power law function, as shown by the black dash-dotted line.

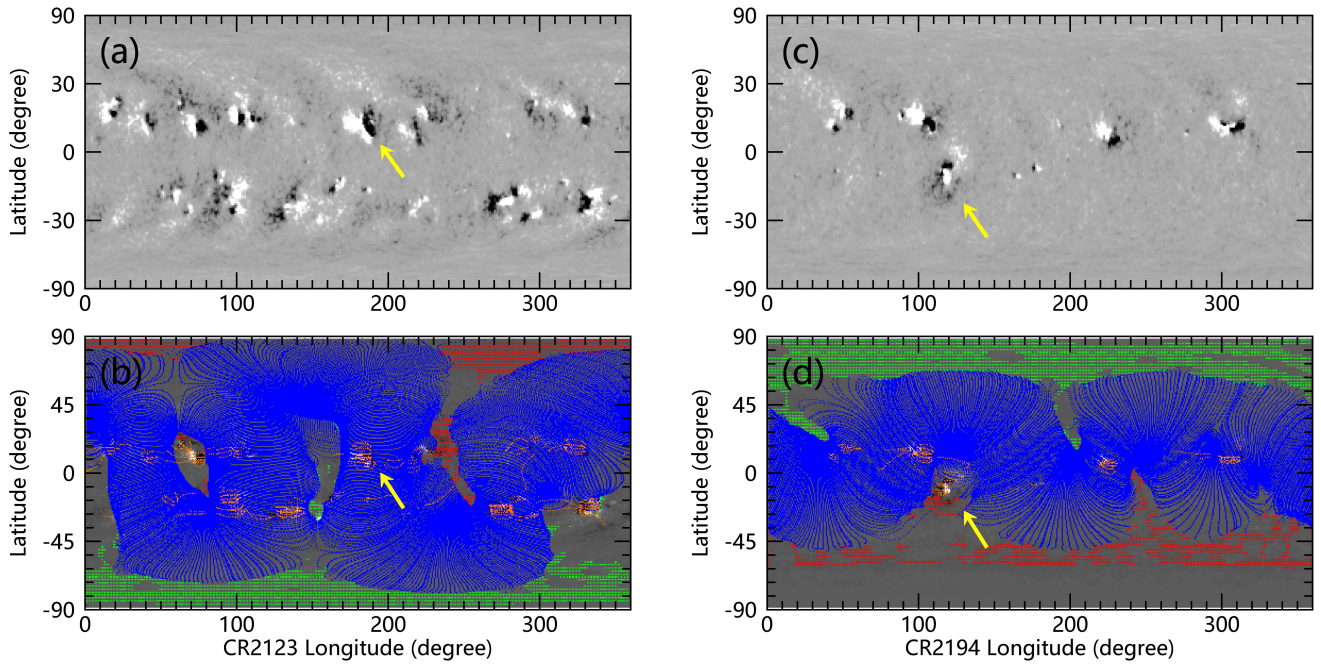


Figure 9. *GONG* synoptic magnetic magnetograms (a, c) and coronal magnetic field by PFSS model (b, d) for Carrington Rotations (CRs) 2123 and 2194. Four categories of field line are plotted: open positive (outward from the Sun) flux in green, open negative flux in red, the tallest closed flux trajectories (indicating the meandering streamer belt) in blue, and closed active region flux in yellow. The yellow arrows point to the active regions of CMEs in the two GLE events on 2012 May 17 (a, b) and 2017 September 10 (c, d), i.e., AR 11476 and AR 12673, respectively.

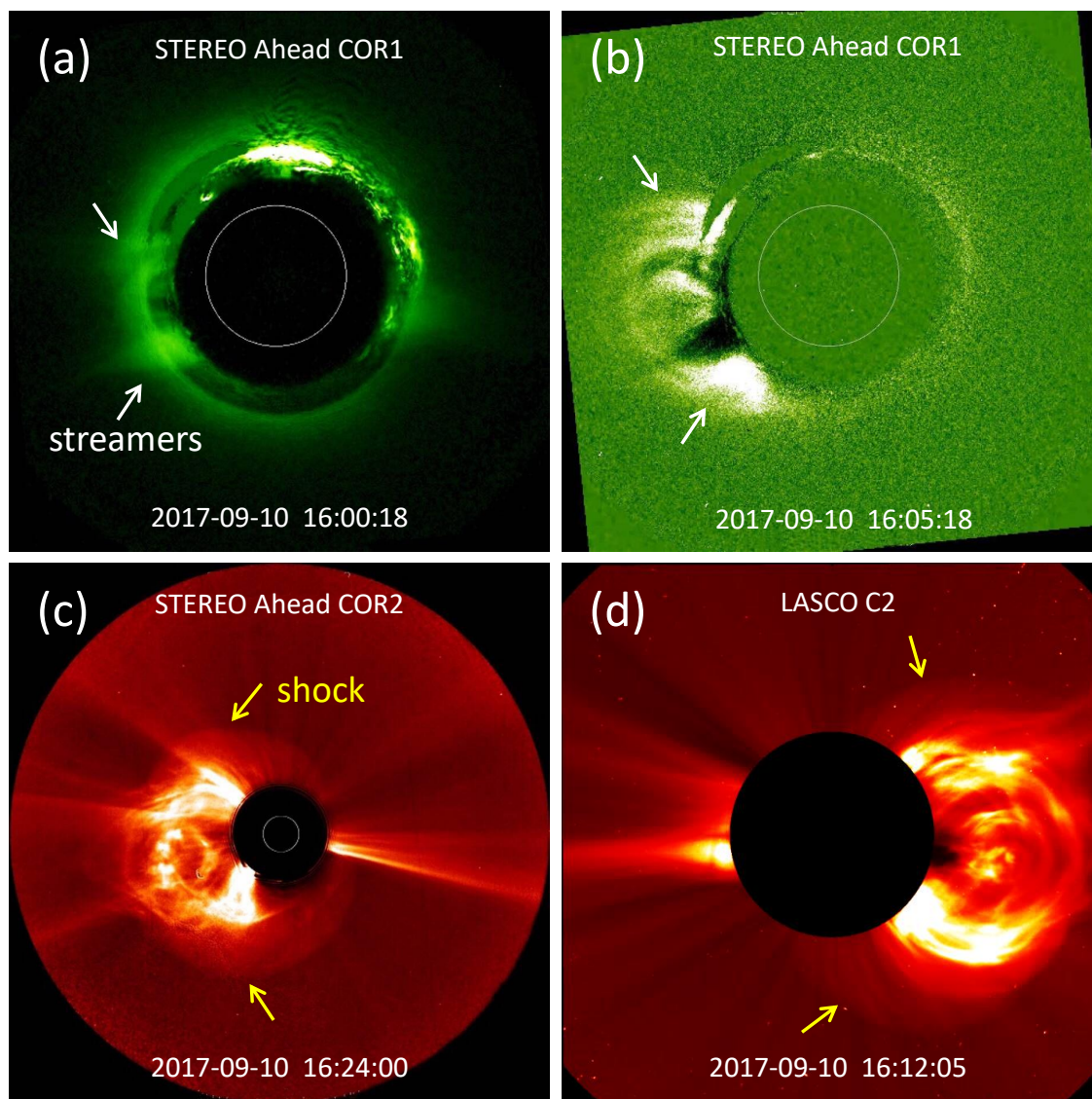


Figure 10. White-light coronagraph observations of the interaction between CME-shock and streamers for the GLE event on 2017 September 10. The white arrows in panels (a) and (b) point to streamers that are strongly deflected by the CME. The yellow arrows in panels (c) and (d) indicate the bubble-shaped structure representing the shock wave front.